

Non-invasive time-resolved measurements of anomalous collision frequency in a Hall thruster

Cite as: Phys. Plasmas **26**, 013516 (2019); <https://doi.org/10.1063/1.5077008>

Submitted: 23 October 2018 . Accepted: 08 January 2019 . Published Online: 31 January 2019

Ethan T. Dale , and Benjamin A. Jorns 

COLLECTIONS

 This paper was selected as an Editor's Pick



View Online



Export Citation



CrossMark

ARTICLES YOU MAY BE INTERESTED IN

[Acceleration region dynamics in a magnetically shielded Hall thruster](#)

Phys. Plasmas **26**, 023506 (2019); <https://doi.org/10.1063/1.5079414>

[Particle-in-cell simulations of Hall thruster acceleration and near plume regions](#)

Phys. Plasmas **25**, 123504 (2018); <https://doi.org/10.1063/1.5054009>

[Tutorial: Physics and modeling of Hall thrusters](#)

Journal of Applied Physics **121**, 011101 (2017); <https://doi.org/10.1063/1.4972269>

Where in the **world** is AIP Publishing?
Find out where we are exhibiting next



Non-invasive time-resolved measurements of anomalous collision frequency in a Hall thruster

Cite as: Phys. Plasmas **26**, 013516 (2019); doi: [10.1063/1.5077008](https://doi.org/10.1063/1.5077008)

Submitted: 23 October 2018 · Accepted: 08 January 2019 · Published Online: 31 January 2019



View Online



Export Citation



CrossMark

Ethan T. Dale  and Benjamin A. Jorns 

AFFILIATIONS

Department of Aerospace Engineering, University of Michigan, Ann Arbor, Michigan 48109, USA

ABSTRACT

The time-resolved cross-field electron anomalous collision frequency in a Hall thruster is inferred from minimally invasive laser-based measurements. This diagnostic is employed to characterize the relationship between the dominant low-frequency “breathing” oscillations and anomalous electron transport mechanisms. The ion Boltzmann equation combined with a generalized Ohm’s law is used to infer key quantities including the ionization rate and axial electric field strength which are necessary in computing the total electron cross-field collision frequency. This is accomplished by numerically integrating functions of velocity moments of the ion velocity distribution function measured with laser-induced fluorescence, in conjunction with current density measurements at a spatial boundary. Estimates of neutral density are used to compute the classical collision frequency profile and the difference in the total collision frequency, and this quantity describes the anomalous collision frequency. This technique reveals the anticipated trends in electron transport: few collisions in the acceleration region but a collision frequency approaching the cyclotron frequency farther downstream. The time-resolved transport profiles indicate that the anomalous collision frequency fluctuates by several orders of magnitude during a breathing cycle. At troughs in the discharge current, classical collisions may dominate; at peaks in the discharge current, anomalous collisions dominate. These results show that the breathing mode and electron transport are directly correlated. This finding is discussed with regard to existing numerical models for the breathing mode and interpretations of anomalous electron transport.

Published under license by AIP Publishing. <https://doi.org/10.1063/1.5077008>

I. INTRODUCTION

Hall thrusters are a class of in-space electric propulsion devices that utilize crossed electric and magnetic fields to produce high thrust and moderate specific impulse compared to alternative electric propulsion technologies. These devices are used extensively for near-Earth commercial and government missions and are increasingly being targeted for deep space applications where their benefits over chemical propulsion can enable new missions.¹ To facilitate these new missions, however, these devices must be long-lived: $\sim 10\,000$ h for recent architectures.² This poses a unique logistical challenge for qualifying this technology for flight.

Despite the extensive and continued flight heritage for Hall thrusters, there are several fundamental aspects of their operation that are not understood. One of the most studied is the so-called anomalous electron transport across magnetic field lines. Classical models of electron transport from the cathode to the anode—those driven by collisions—underpredict the experimentally measured electron current flowing in the device by orders

of magnitude. This suggests that there must be an anomalous (non-classical) transport mechanism somehow enhancing this current. The physical nature of this anomalous electron transport and the mechanism responsible for it remain a prominent and unresolved topic of Hall thruster research.³ As a result of the current lack of first-principles understanding of this process, it has not been possible to implement a self-consistent, predictive Hall thruster numerical model to date. Such a tool is highly desired for use in analysis and predictive design of Hall thrusters. For example, simulation can be used to avoid the logistical complications of ground testing⁴ for new thrusters or new missions.

The importance of the electron dynamics to a thruster’s fundamental operation has given rise to a concerted effort to study it numerically, experimentally, and analytically. The numerous investigations that have been conducted on anomalous electron transport have led to a number of different theories for the mechanisms that might drive it. These include wall collision effects,⁵ coherent instabilities,⁶ or turbulence.⁷ Often, reduced dimensional numerical simulations aid the study of

these different effects.^{7–9} These codes are used to identify if the criteria are met for the onset of proposed transport mechanisms and whether a given mechanism drives transport in real devices with similar geometry. While these types of numerical investigations are critical for understanding the physical processes governing electron transport, the ultimate benchmark for evaluating different theories is direct experimental assessment of the anomalous electron transport inside an actual thruster.

With this in mind, there have been a number of attempts at measuring electron mobility experimentally. The most direct attempts used *in situ* probes.¹⁰ Although these measurements were simple to execute and yielded qualitative insight into the magnitude and spatial distribution of the electron transport, their results must be understood in light of the fact that near-field electrostatic probing has been shown to be highly perturbative.^{11–13} Probe measurements thus likely do not accurately reflect the behavior of the unperturbed discharge. As a less invasive alternative, electron dynamics can be inferred through a numerical inversion scheme in which iterative numerical experiments can be performed to determine transport profiles by matching code results with various experimental measurements (e.g., discharge current or thrust).¹⁴ The major reservation for this approach, however, is that the transport profiles inferred in this way may not necessarily represent a unique solution and can be highly sensitive to how the inversion is done (cf. Ref. 15). The shortcomings of this technique and *in situ* probing underscore the point that there is a need for less invasive experimental measurements of electron transport.

As an additional consideration, both numerical and experimental methods to measure the anomalous electron dynamics often fail to capture the evolution of anomalous transport over time, due to either the source of empirical transport parameters, the inability of a code to reproduce time-dependent behavior, or the constraints of the diagnostic. This is potentially a considerable limitation given that Hall thrusters are highly dynamic.¹⁶ For example, low-frequency global oscillations called the “breathing mode” are ubiquitous in Hall thrusters and can be very strong, with discharge current fluctuations in excess of 100% (peak-to-peak) of the mean. With such a significant influence on the thruster dynamics, it is reasonable to expect the electron transport to be influenced by this instability. However, the nature of this relationship is still poorly understood. For example, a number of numerical treatments have considered the anomalous collision frequency to be constant in time. The oscillations reproduced by these codes have limited validation against experimental measurements of the breathing mode, and these codes sometimes predict the existence of spurious oscillations that are not experimentally observed.¹⁷ Interestingly, there are other codes¹⁸ where a constant collision frequency is assumed and yet they do predict oscillations similar to the breathing mode. In either case, given that how current and electron transport are linked, it is not unreasonable to expect that a full understanding of how these properties are related is critical for self-consistently modeling the large-scale breathing oscillations.

In summary, there is a need for both non-invasive and time-resolved experimental measurements of electron transport quantities to help inform numerical simulations, provide

critical benchmarks for first-principles analysis, and explore the connection between low-frequency oscillations and electron transport behavior. Furnishing these measurements will not only directly increase code fidelity by providing more realistic transport data but can also yield insight into the underlying mechanisms governing anomalous transport. In this paper, we present a novel, minimally invasive, time-resolved technique for measuring the anomalous electron dynamics in a Hall thruster. In the first section, we formulate the problem of anomalous electron dynamics in Hall thrusters in terms of a scalar parameter, an anomalous collision frequency acting to drive cross-field transport. This is following the treatments of several others.^{19–21} Framed in this context, we then describe our technique for measuring this anomalous collision frequency directly employing a combination of laser and probe-based diagnostics. This is followed by a description of the experimental setup for implementing this technique on a laboratory Hall thruster. We then present the results from this setup for measurements of the electron collision frequency as a function of position and time. We conclude with a discussion about the benefits and limitations of this technique as well as the implications of our findings on the relationship between electron transport and low-frequency oscillations in these devices.

II. APPROACH

In this section, we review how the problem of anomalous electron transport can be formulated in terms of an anomalous electron collision frequency. We then describe what experimental measurements are necessary to calculate this anomalous collision frequency.

A. Anomalous collision frequency

Hydrodynamic representations of Hall thrusters treat electrons as a fluid where conservation of momentum neglecting electron inertia is encapsulated by Ohm’s law

$$\vec{E} = \eta_e \vec{j}_e + \eta_e \Omega \vec{j}_e \times \hat{\beta} - \frac{\nabla p_e}{n} + \eta_i \vec{j}_i. \quad (1)$$

Here, η_e is the electron resistivity, η_i is the resistivity due to classical ion collisions, \vec{j}_e is the electron current density, and \vec{j}_i is the ion current density. The resistivities are generally defined as $m\nu/q^2n$ and the current densities as qnu . The Hall parameter Ω is the ratio of the cyclotron frequency $\omega_{ce} \equiv qB/m_e$ and total electron collision frequency ν_t . The electron pressure p_e is given by enT_e , where T_e is the electron temperature in eV. In the canonical Hall thruster architecture, the plasma is contained in an annular ceramic channel of width w and length L with an anode serving as a gas distributor at the back of the channel and a cathode near the axis of symmetry, as shown in Fig. 1. The electric field $\vec{E} \approx E_z \hat{z}$ is mostly axial and the magnetic field $\vec{B} = B \hat{\beta} \approx B_r \hat{r}$ is mostly radial. The balance of forces in Ohm’s law includes the electric force, pressure, Lorentz force, and a collisional drag. This drag is classically the result of electron-ion and electron-neutral collisions. Anomalous transport can be represented in Ohm’s law as an additional drag force \vec{F}_a formulated such that $\vec{F}_a = (m_e/q^2)n\nu_a \vec{j}_e \equiv \eta_a \vec{j}_e$, where the anomalous drag is ascribed to an anomalous collision frequency ν_a . The total

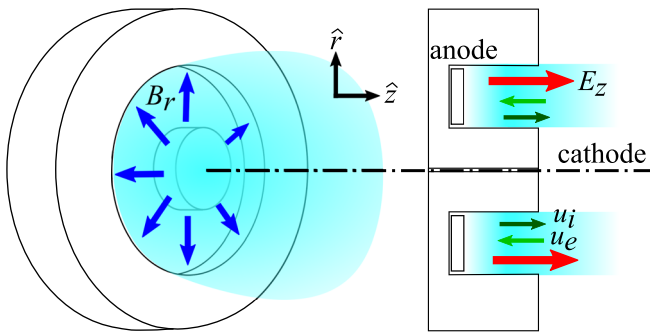


FIG. 1. The configuration considered for the mobility calculations in this study.

drag in Eq. (1) is therefore $(\eta_e + \eta_a)\vec{j}_e \equiv \eta_t\vec{j}_e$, where the total resistivity η_t is a function of ν_t , the sum of classical collisions ν_{class} and anomalous collisions ν_a . Anomalous transport can be directly characterized within this framework if the total electron collision frequency and the classical collision frequency can be measured.

To determine the total collision frequency, the axial component of Eq. (1) is taken

$$E_z = \eta_e j_e (1 + \Omega^2) - \frac{\nabla p_e}{n} + \eta_i j_i. \quad (2)$$

The first term on the right-hand side is the resistivity due to electron collisions in the presence of a magnetic field; the second term is the electron pressure gradient, which generates an electric field when there are large electron density or temperature gradients, such as near the magnetic barrier in a Hall thruster; and the last term is the ion resistivity due to ion collisions. Equation (2) is quadratic in ν_t such that

$$\nu_t = \frac{\mathcal{E} \pm \sqrt{\mathcal{E}^2 - (2u_e B_r)^2}}{2 \frac{m}{e} u_e}, \quad (3)$$

where u_e is the electron velocity and we have defined $\mathcal{E} \equiv E_z + \frac{\nabla p_e}{n} - \eta_i j_i$. Physically, \mathcal{E} represents the electric field due solely to electron collisional resistivity according to Eq. (2). If ion resistivity and electron pressure were neglected, \mathcal{E} would be identical to E_z . The total collision frequency given in Eq. (3) includes all collisions that electrons may undergo while transiting the thruster: anomalous collisions, electron-neutral collisions ν_{en} , and electron-ion collisions ν_{ei} .

Armed with Eq. (3), we can evaluate the total collision frequency if plasma density, electron temperature, electron and ion velocity, axial electric field, and radial magnetic field are known. While there are standard techniques for determining most of these properties, to date it has not been possible in Hall thrusters to measure the electron velocity directly. As an alternative approach following the work of Linnell,²² we instead make a series of approximations that allow us to relate this parameter to the more easily measured values of ion and discharge currents. To this end, noting that radial currents in a Hall thruster are small or symmetric²³ and assuming radial symmetry

within the channel such that gradients in the radial direction are small on the centerline, we can treat the ion and electron continuity equations as effectively one dimensional in the axial direction. This allows us to express the electron current density in the axial direction as the difference in total (discharge) current density and ion current density, $j_e = j_d - j_i$. The ion current density can be calculated from the plasma density and ion mean velocity \bar{u} , which can be measured directly and assumed one-dimensional due to the ballistic nature of ions and small divergence of the ion beam in the near field. The discharge current density j_d can be calculated from the discharge current I_d and the known channel area A if it is assumed that current is carried uniformly across the channel, i.e., $j_d = I_d/A$. Alternatively, a non-uniform shape to the current distribution could be inferred from numerical simulations or otherwise assumed, but without knowing the distribution and its evolution over a breathing cycle exactly, such an approach could be just as inaccurate as assuming a uniform distribution. This assertion will be discussed further in Sec. VB. With these approximations, Eq. (3) thus reduces to

$$\nu_t = \frac{\mathcal{E} \pm \sqrt{\mathcal{E}^2 - \left[2 \left(\frac{j_d}{n} - \bar{u} \right) B_r \right]^2}}{2 \frac{m}{e} \left(\frac{j_d}{n} - \bar{u} \right)}. \quad (4)$$

In this form, it is possible to evaluate the total collision frequency by using standard diagnostic techniques to measure typical plasma parameters in the thruster, e.g., density and electric field. The anomalous collision frequency ν_a in turn can be found by subtracting the classical contributions, ν_{ei} and ν_{en} , from ν_t (cf. Ref. 24).

The measurement of collision frequency with Eq. (4) has already been done with physical probing techniques in a time-averaged way.²² However, as we discussed in Sec. I, these techniques were perturbative and did not yield any information on the dynamic response of the plasma. Our approach to measuring these parameters differs in the present investigation in that we use a weakly invasive technique to acquire them. The method for this is outlined in Sec. IIB.

B. Boltzmann method

The evaluation of Eq. (4) requires measurements of several local plasma parameters in the thruster discharge including E_z , ionization rate n_0 , \bar{u} , n , B_r , and j_d . The first three listed quantities can be computed from measurements of the ion velocity distribution function (IVDF) using moments of the Boltzmann equation, as described by Pérez-Luna *et al.*²⁵ The magnetic field for a given thruster is known by design, and the discharge current density can be estimated from I_d which is measured non-invasively as part of typical thruster telemetry. This leaves only the plasma density and neutral density as unknowns. We detail in the following how these latter quantities can also be computed by extending the Boltzmann method of Pérez-Luna *et al.*

The one-dimensional Boltzmann equation for ions dictates the evolution of the IVDF, f , over time due to convection, applied forces, and ionization

$$\frac{\partial f}{\partial t} + u \frac{\partial f}{\partial z} + \frac{e}{m} E_z \frac{\partial f}{\partial u} = \nu_{iz} f_0. \quad (5)$$

Here, u is the independent ion velocity, not the mean velocity \bar{u} . In the term on the right-hand side, ν_{iz} is the ionization frequency and f_0 is the newborn IVDF. The product of these terms is the ionization rate with dimensions of particles born per volume per time. Taking the zeroth, first, and second moments of Eq. (5) produces the familiar fluid equations for ions

$$\frac{\partial n}{\partial t} + \frac{\partial \bar{u}n}{\partial z} = \dot{n}_0, \quad (6)$$

$$\frac{\partial \bar{u}n}{\partial t} + \frac{\partial \bar{u}^2 n}{\partial z} - \frac{e}{m} n E = 0, \quad (7)$$

$$\frac{\partial \bar{u}^2 n}{\partial t} + \frac{\partial \bar{u}^3 n}{\partial z} - 2 \frac{e}{m} n E \bar{u} = 3 \frac{e}{m} T_i \dot{n}_0, \quad (8)$$

where $\bar{w} = \int w^3 f du / n$. Equations (6)–(8) represent continuity, momentum conservation, and energy conservation for ions, respectively. If the IVDF is known at all positions and times, the only unknowns in the system of Eqs. (6)–(8) are the electric field, ionization rate, density, and newborn ion temperature T_i . The last quantity can be approximated as the neutral gas temperature which is expected to be negligible compared to the ion velocity at most locations, leaving only the first three listed quantities as unknowns. As a result, Eqs. (6)–(8) represent a system of three equations with three unknowns that can be solved for explicitly given adequate boundary conditions. In the work of Pérez-Luna *et al.*, only the steady case was considered, which simplified the governing equations significantly. These equations became ordinary differential equations with position as the independent variable; they only required steady-state boundary conditions; and because the time-dependent terms vanish, n dropped out of the equations and thus an evaluation of the IVDF second moment \bar{u}^2 was required rather than the third moment as shown in Eq. (8).

However, here we are interested in the time-resolved solution of these governing equations. In this case, Eqs. (6)–(8) can be solved explicitly for \dot{n}_0 , E_z , and $\partial n / \partial x$. The density at all times and axial positions can then be determined by marching upstream and integrating $\partial n / \partial x$ given a boundary measurement of density over time at a single location. Physically, this approach solves the ion continuity, momentum conservation, and energy conservation equations numerically such that the population is not assumed to be Maxwellian and thus the solutions are dependent on velocity moments.

This Boltzmann moment method therefore allows E_z , \dot{n}_0 , and n to be computed when the normalized IVDF is measured at all times and locations, and a boundary measurement of density is made as a function of time. By virtue of these measurements, \bar{u} is also known. The only remaining quantity that must be determined to compute ν_t is neutral gas density. Many numerical simulations treat the neutral gas with a particle-in-cell (PIC) approach, using a Monte Carlo scheme or a macroparticle weighting algorithm for ionization.²⁰ Alternatively, a simpler approach would be to apply fluid equations to the neutral population. Neutral laser-induced fluorescence experiments on a 6-kW Hall thruster²⁶ have indicated that the velocity distribution

is roughly Maxwellian throughout the channel. This would seem to suggest that the fluid approximation can be applied. With that said, that work as well as others²⁷ have shown that kinetic effects cannot entirely be ignored and do play a role in neutral gas dynamics in a Hall thruster channel. We choose to neglect these kinetic effects in this study for the sake of simplicity and justify this assumption by noting that the neutral density is anticipated to vary within an order of magnitude in the channel,²⁶ while the anomalous collision frequency may be several orders of magnitude greater than ν_{en} .

The collisionless neutral continuity and momentum conservation equations, assuming evenly dispersed gas from the anode such that the flow can be considered one-dimensional, are

$$\frac{\partial n_n}{\partial t} + \frac{\partial \bar{u}_n n_n}{\partial x} = -\dot{n}_0, \quad (9)$$

$$\frac{\partial \bar{u}_n n_n}{\partial t} + \frac{\partial \bar{u}_n^2 n_n}{\partial x} = 0. \quad (10)$$

The neutral density and velocity can be computed from these equations (with the ionization rate coming from the ion Boltzmann analysis from before) provided that we have boundary measurements of the neutral density and velocity over time. In this study, we assume that neutral fluctuations are damped downstream of the exit plane due to the expansion of the gas into vacuum, and so, a steady density and velocity were used. The boundary conditions were guided by experimental measurements in the literature²⁶ and chosen specifically to produce a stable solution, with the boundary density self-consistently calculated for a known anode flow rate by a mass conservation argument. We discuss the sensitivity of our solution to these assumptions in Sec. VA.

In summary, we have shown that it is necessary to measure E_z , \dot{n}_0 , \bar{u} , n , n_n , B_r , and j_d to determine the electron anomalous collision frequency profile experimentally. The Boltzmann moment analysis for ions yields E_z , \dot{n}_0 , \bar{u} , and n , while neutral fluid equations utilizing the computed \dot{n}_0 provide n_n . As stated previously, B_r and j_d are readily and non-intrusively measured or estimated. Using the techniques described in this section, measurements of the time-resolved IVDF inside and in the near plume of a Hall thruster, coupled with boundary measurements of density, are sufficient to experimentally characterize electron transport. In Sec. III, we describe the practical aspects of executing this technique.

III. EXPERIMENTAL SETUP

In this section, we review the details of applying the technique presented in Sec. II. We first describe the thruster being studied and the facility in which it was operated. We then review the method by which the IVDFs and boundary ion densities were measured: time-resolved laser-induced fluorescence (TRLIF) and Faraday probing, respectively.

A. Thruster and facility

The experiment was conducted at the University of Michigan in the Large Vacuum Test Facility (LVTF), a 6-m

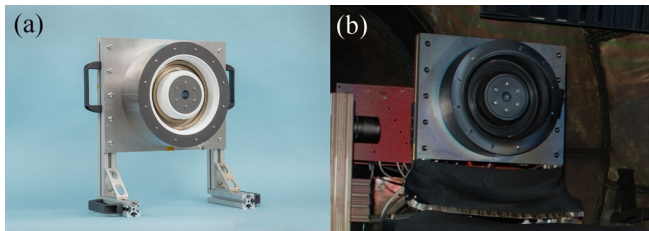


FIG. 2. The H9 thruster soon after manufacture (a) and in an experimental configuration in the LVTF (b).

diameter 9-m long stainless steel-clad vacuum chamber. For this study, the LVTF was pumped with five copper cryogenic “thumpers” and eight LN₂-baffled TM-1200 cryogenic pumps. The chamber reached a base pressure below 1 μ Torr-N₂ and the measured pumping speed on xenon was approximately 300 kL/s. The pressure in the chamber was measured with a MKS 370 Stabil-Ion gauge equipped with a neutralizer and mounted roughly 1 m from the thruster, as recommended by Dankanich *et al.*²⁸

The thruster tested in this experiment was the H9, a 9-kW magnetically shielded Hall thruster developed collaboratively by the Jet Propulsion Laboratory, the University of Michigan, and the Air Force Research Laboratory. Figure 2 shows the thruster after manufacture and installed in the LVTF. The thruster’s design and initial performance have been described in Refs. 29 and 30. The magnetically shielded topography is not anticipated to influence the breathing behavior of the thruster, as other studies have shown qualitatively similar oscillations between shielded and unshielded devices.³¹ The thruster was run with a 20-A lanthanum hexaboride hollow cathode, mounted centrally and operated at 7% of the anode flow. The thruster was run on 99.9995% pure xenon at 300 V and 2.5 kW. The background pressure during operation was approximately 4 μ Torr-Xe. The thruster body was manually set to cathode potential (“cathode-tied” configuration) and the current collected by the body was found to be \sim 6% of the discharge current.

We chose this 2.5 kW operating condition because the thruster exhibited strong (100% peak-to-peak) but coherent discharge current oscillations, as demonstrated in time and frequency space in Fig. 3. The peak frequency in the discharge current spectrum varied from 15 kHz during measurements of

the IVDFs to 11 kHz during measurements of boundary ion density. It is possible that the proximity of the Faraday probe in the latter measurements slightly perturbed the thruster, leading to the change in frequency. However, the average discharge current did not change significantly and the shape of the discharge current signal remained the same between measurements. To compensate for the change in frequency, the data in Sec. IV will be presented as a function of breathing phase (in degrees) rather than time.

Although this is an unusually low-power operating condition for the H9, it is in fact within its designed operating envelope according to Ref. 29. However, we can still consider the extensibility of any measurements made here to higher-power conditions that are more typical of the H9. Previous work on a similar but unshielded thruster³² has shown remarkably similar potential structures (reflected by the mean ion velocity profile) across a wide range of operating conditions, including those similar to the 2.5 kW condition used in the present experiment. Further, discharge current typically scales linearly with propellant flow rate in modern Hall thrusters, the H9 included,³⁰ and so operating at below-nominal discharge power is not expected to drastically change the physical processes governing electron transport.

B. IVDF measurements

Laser-induced fluorescence (LIF) is a diagnostic commonly used in Hall thruster studies to measure normalized IVDFs.³³ In this experiment, the non-resonant $5d[4]_{7/2} - 6p[3]_{5/2}$ transition was exploited in the following way. First, laser light detuned from the stationary transition wavelength is focused axially to a roughly 1 mm³ point in the discharge. The wavelength is measured precisely with a wavemeter. At the interrogation point inside the discharge, the laser wavelength Doppler shifts to the stationary wavelength in the frame of reference of ions at a specific velocity. These ions are excited by the laser, and the subsequent fluorescence is collected with optics offset from the thrust axis by 60°. The fluorescence is filtered with a monochromator, amplified with a photomultiplier tube and trans-impedance amplifier, and finally homodyned with a lock-in amplifier to discriminate the fluorescence from background light. By detuning the laser over a range of wavelengths, the relative population density over a corresponding range of

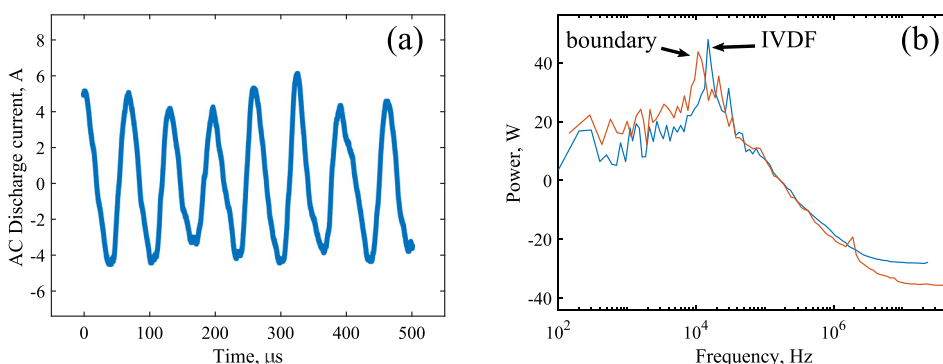


FIG. 3. A representative discharge current signal in time (a) and the spectra (b) during boundary density measurements (“boundary”) and IVDF measurements (“IVDF”).

velocities can be determined. The normalized curve that results is approximately equal to the ion velocity probability function, which is equivalent to the IVDF normalized by the local density. The effect of saturation—pumping the excited state faster than it can fluoresce—was explored by varying laser powers and examining the change in fluorescence intensity, and the response was found to remain linear throughout the range of laser powers tested. The Zeeman effect may also broaden the IVDF by splitting the fluorescence line. The uncertainty due to this effect was calculated in the fashion of Huang *et al.*²⁶ and Jorns *et al.*,³⁴ and assuming Gaussian normalized IVDFs, we found it to contribute <10% uncertainty to the computed velocity moments at all times within the entire LIF domain, <1% at the exit plane, and even less downstream. Figure 4 shows a diagram of the LIF setup inside the chamber.

While several methods have been developed for performing time-resolved laser-induced fluorescence (TRLIF) measurements, we elected to use one of the simplest for implementation in this study: boxcar averaging.³⁵ An SRS SR250 gated integrator filtered the fluorescence signal before homodyning it with a lock-in amplifier. The gated integrator was triggered with the discharge current signal, outputting the fluorescence signal within a 10 μs gate and a computer-controlled delay once triggered. By varying the gate delay throughout a breathing period, the fluorescence at specific phases of a breathing cycle was sampled. We evenly sampled ten phases between 0 and 65 μs of delay. The chosen gate width dictated a Nyquist frequency of 50 kHz, which is sufficient to resolve the breathing frequency in this experiment. For our time-resolved LIF measurements, the spatial resolution was 5 mm far upstream and downstream and 1 mm near the exit plane where ion velocity gradients were anticipated to be large.

C. Boundary density measurements

The boundary density measurements were made with an *in situ* Faraday probe at the most downstream (least perturbative) TRLIF acquisition location. This probe consisted of a 4.8 mm²

planar graphite electrode housed within a 30 cm alumina tube. The probe was sized to collect a very small fraction of the discharge current and obscure very little of the beam while still being large enough to develop a thin sheath and thus suffer little from the absence of a guard electrode. At the downstream edge of the TRLIF domain, the Debye length was approximately 50 μm or about 57 times smaller than the probe diameter. The probe was biased between -25V and -30V to ensure that only ion current was collected. Although the probe bias was not varied widely to verify that ion current was saturated at the chosen values and thus sheath effects were minimal, nearby Langmuir probe measurements yielded mean plasma density values within 25% of the average time-resolved Faraday probe measurements. This implies that these measurements are realistic and not heavily skewed by sheath effects. The probe was swept into the beam at 50 cm/s with a linear motor as shown in Fig. 4, and the current collected by it was measured with a small shunt resistor and a high-speed digitizer. The current density encountered by the probe j_i was calculated using the measured area of the collector. The mean ion velocity at that location was extracted from the coincident TRLIF measurements, allowing the density to be computed as $n = j_i/\bar{u}$. Figure 5 shows the Faraday probe tip before and after testing.

IV. RESULTS

The total collision frequency computed with the technique of Sec. II is shown at various phases of the breathing mode in Fig. 6. Also included at the same ordinate scale is the classical collision frequency at these phases. At the minimum in discharge current (denoted “3”), the total collision frequency is nearly equal to the classical collision frequency, while at the peak in discharge current (“1”), there is an order of magnitude or greater difference between them. This indicates that the anomalous collision frequency—the difference between the curves in Figs. 6(b) and 6(c)—fluctuates significantly throughout a breathing cycle and even becomes negligible at times. It is also interesting to observe that the local minimum in collision frequency nearly coincides with the peak electric field strength but is

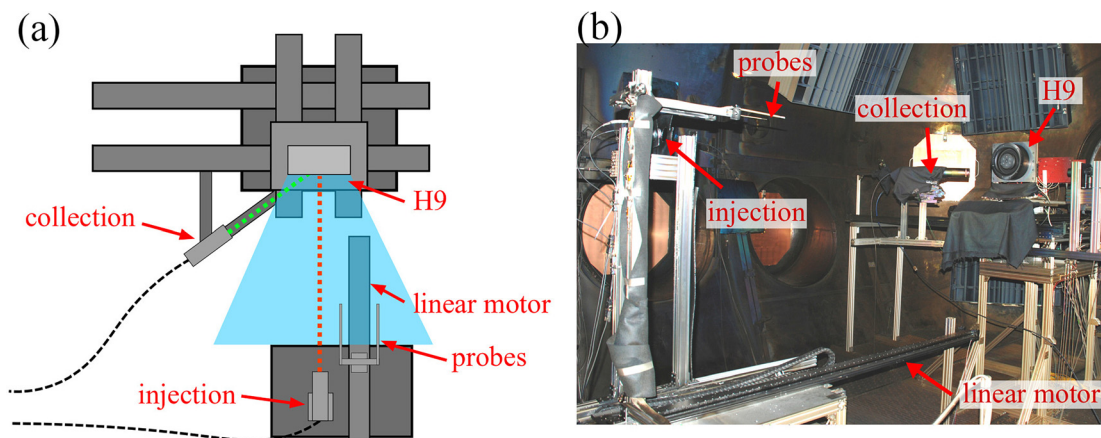


FIG. 4. The experimental setup inside LVTF, shown with a birds-eye diagram (a) and a photo (b). The collection and injection optics were used for LIF measurements, and the linear motor and probes were used for Faraday probe measurements.

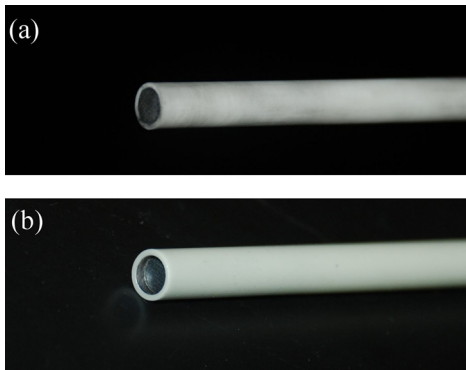


FIG. 5. The Faraday probe used for boundary density measurements, before testing (a) and after testing (b).

consistently upstream of the location of maximum radial magnetic field. The fact that the electric field peak was located upstream of the location of the peak magnetic field was also evident in dedicated time-averaged LIF measurements, and this shift in position is much too large to be explained by uncertainty in the axial position of the thruster. This contrasts with steady-state measurements that show the two to be nearly coincident in other thrusters, both shielded like the H6MS³⁶ and unshielded like the H6,³² as well as others.^{13,37} The reason why this discrepancy occurs compared to similarly configured devices is not immediately apparent, although previous studies³⁸ on a 12.5-kW magnetically shielded thruster have shown the acceleration region to shift upstream as the radial magnetic field increases. This may imply that the magnetic field used for the operating condition in the present study was relatively strong for the power level.

Figure 7 shows several of the constituent quantities used to calculate ν_t . Included are the electric field strength, electron pressure gradient, plasma density, electron temperature, and current densities. It shows that the electric field is the strongest at the discharge current minimum and weakest at its maximum. In contrast, the total collision frequency and the electron current density are generally weakest at the discharge current

minimum. This implies that either the increase in resistivity is relatively more than the decrease in j_e or the electron pressure gradient increases dramatically as discharge current reaches a minimum. Figure 7(b) indicates that the electron pressure gradient peak magnitude increases with decreasing discharge current, but by only about 200 V/cm at most, while E_z increases by about 400 V/cm in some locations. Thus, changes in resistivity must be contributing significantly to the fluctuation of electric field strength, and therefore, resistivity is especially sensitive to the fluctuations of discharge current during a breathing cycle. This observation is a strong piece of evidence that breathing fluctuations are highly correlated with electron transport. Additionally, the plots show that the ion current density fluctuates much less than the electron current density, suggesting that the breathing oscillations have more impact on electron transport than ion transport.

Figure 8 shows the mean total and classical collision frequency profiles calculated by averaging the time-resolved results over a breathing period. The ν_t curve is surrounded by a region of boot-strapped 95% statistical uncertainty, which is also representative of the error for the data in Fig. 6. Figure 8 also shows the average electric field, electron pressure gradient, plasma density, electron temperature, and current densities. A local minimum in the collision frequency exists near the average location of the peak electric field, which agrees with experimental measurements of Linnell and Gallimore²² and a semi-empirical mobility model synthesized by Koo and Boyd.⁹ Further, the total collision frequency appears to begin approaching the classical frequency upstream, which agrees with fluid simulations with the Hall2De code.¹⁴ Finally, the peak mean electron temperature is close to the anticipated value of 30 eV according to a common heuristic that dictates T_e to be approximately 10% the discharge voltage.²⁴

It is important to note that ν_t shown in Figs. 6 and 8 has been given a minimum bound of ν_{class} , but at certain locations and phases, Eq. (3) yields a raw collision frequency less than the classical value, which implies a negative anomalous electron drag. As this is physically unrealistic, this discrepancy indicates that either the assumptions of Sec. II B are poor or the uncertainty in ν_t exceeds the classical collision frequency. Although

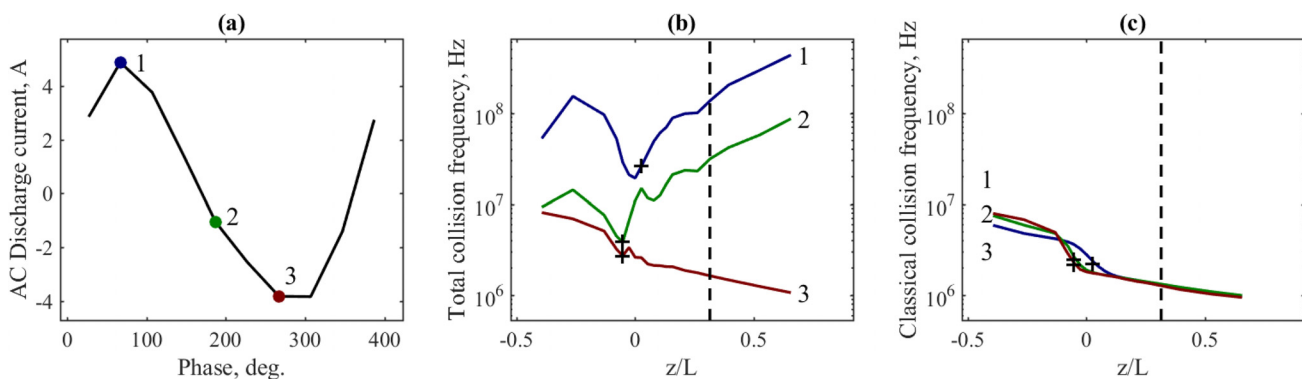


FIG. 6. The discharge current (a), total collision frequency (b), and classical collision frequency (c) at three representative phases of the breathing cycle. The location of the maximum radial magnetic field is indicated with a vertical dashed line, and the location of peak electric field strength is indicated with a “+.”

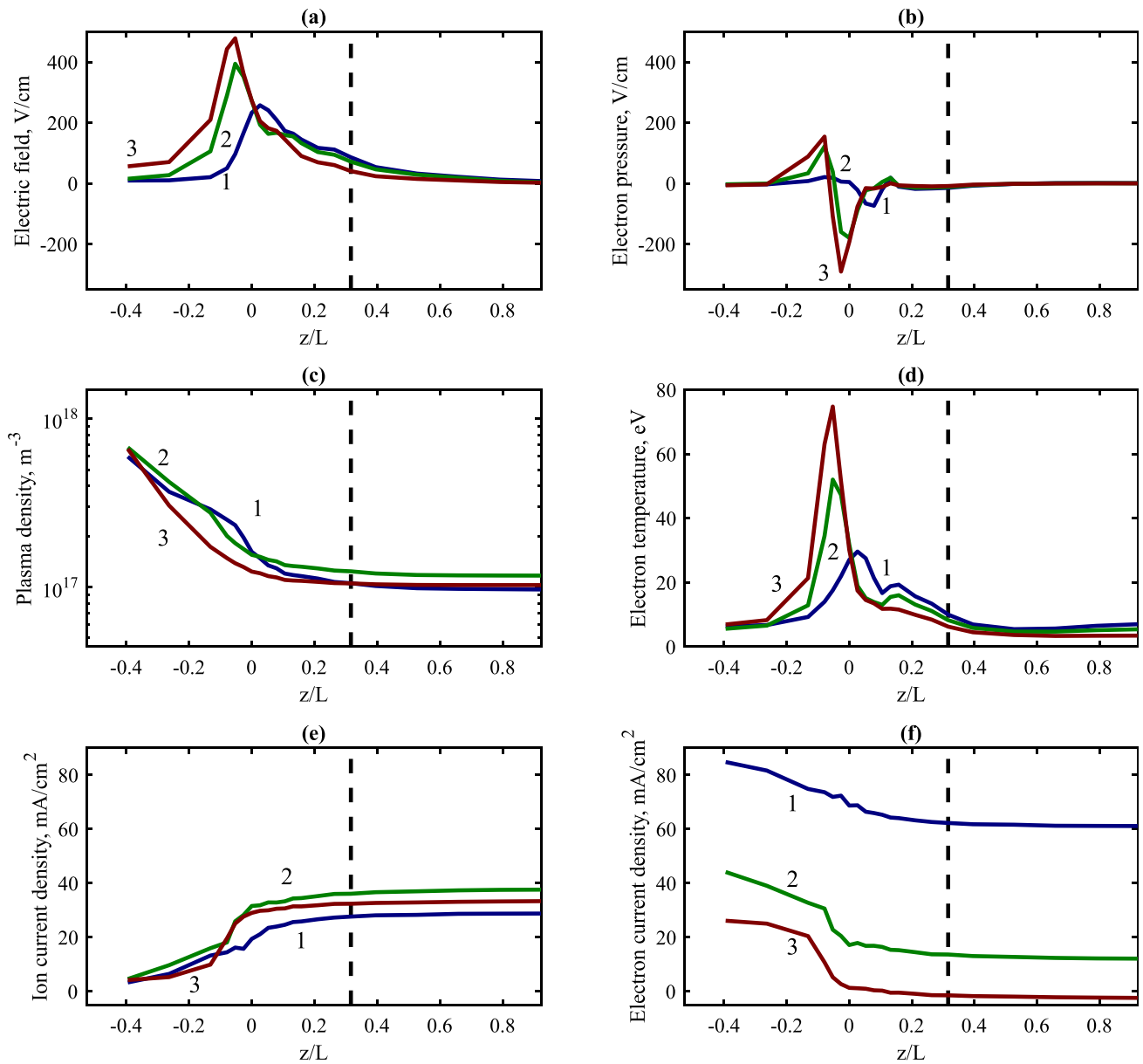


FIG. 7. The (a) axial electric field strength, (b) electron pressure gradient, (c) plasma density, (d) electron temperature, (e) ion current density, and (f) electron current density at phases of the breathing cycle corresponding to those in Fig. 6. The location of the maximum radial magnetic field is indicated with a vertical dashed line.

the uncertainty can be large for ν_t , it is not comparable to ν_{class} according to Fig. 8. The only remaining explanation then is that assumptions underpinning the technique used to compute these quantities have been violated at the points where $\nu_t < \nu_{class}$. This and other limitations will be discussed further in Sec. V.

V. DISCUSSION

In this section, we first review the sensitivity of the neutral gas calculations to the chosen boundary values. Next, we discuss the validity of other major assumptions in the Boltzmann

method proposed and applied in this study. We then discuss the broader ramifications of our findings for approaches to Hall thruster simulations. Finally, we conclude by examining the relationship between breathing and anomalous transport based on the results of Sec. IV.

A. Neutral density calculation

Many of the results in Sec. IV depend on neutral density, which was calculated via continuity and momentum

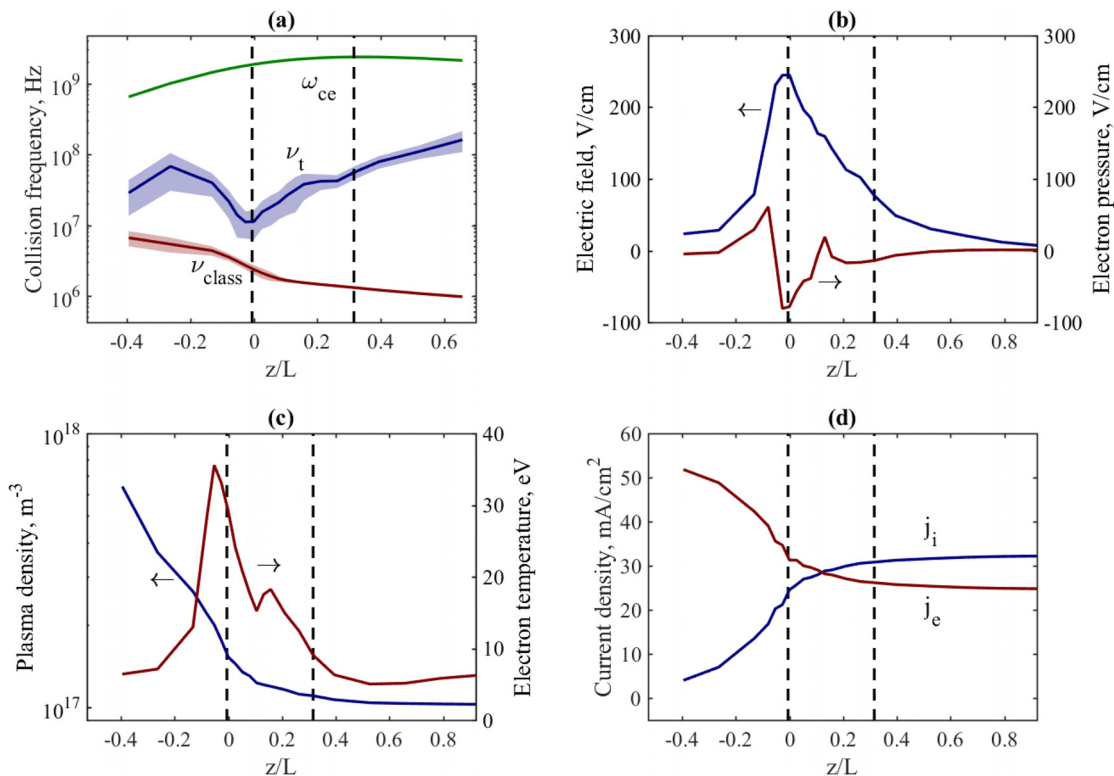


FIG. 8. (a) The mean total and classical collision frequencies and their statistical uncertainty regions, (b) the mean electric field and electron pressure gradient, (c) the mean plasma density and electron temperature, and (d) the mean current densities. The location of the maximum radial magnetic field is indicated with the right vertical dashed line, and the average location of peak electric field strength is indicated with the left vertical dashed line. Horizontal arrows indicate the relevant ordinate for each curve.

conservation self-consistently with the ionization rate computed with the Boltzmann moment method. The boundary conditions for this approach were not the result of direct measurements in this experiment, and thus, consideration must be given to the sensitivity of the resulting neutral density profiles to these boundary conditions. The specific values for downstream neutral density and velocity corresponding to the operating condition described in Sec. III A were $1.2 \times 10^{18} \text{ m}^{-3}$ and 600 m/s, respectively. The magnitude of the resulting neutral density profile is indeed sensitive to the choice of the boundary velocity above 600 m/s, but this sensitivity is mild in a logarithmic sense. For example, increasing the boundary velocity by 50% leads to at most a 50% change in the neutral density at any point and on average a 35% change. This change in density corresponds to less than a third of an order of magnitude, while the neutral density spatially varies by roughly an entire order of magnitude consistently through a breathing cycle. In this way, the relationship between ν_t and ν_{class} is not expected to be significantly impacted by the choice of boundary velocity.

B. Boltzmann method assumptions

As a review, the major theoretical and practical assumptions of the method used in this study are as follows:

- Ion behavior is sufficiently ballistic that it can be approximated as one-dimensional.
- Ion collisions are negligible compared to ionization effects.
- Perturbations due to the Faraday probe proximity are minimal such that the resulting current density measurements are accurate.
- Current is conserved one-dimensionally inside and in the near-field of the thruster.
- Discharge current density can be approximated as an average value (radially uniform current distribution).
- Neutral particles can be treated as a Maxwellian fluid, mediated by either self-collisions or wall collisions.
- The neutral density and flow rate are constant in time in the downstream near field of the thruster.
- Electrons are Maxwellian and move one-dimensionally in the near field.

There are several major aspects of these assumptions that must be discussed in context of the results of Sec. IV. First, we consider the analytical limitations of Eq. (3). Given that on physical grounds ν_t must be greater than zero, the form of Eq. (3) has two requirements: (1) \mathcal{E} and u_e must have the same sign and (2) $\mathcal{E} \geq 2u_e B_r$ such that ν_t is real. The latter inequality provides a lower bound on the magnitude of \mathcal{E} , at which point the total collision frequency for electrons is the cyclotron frequency

(demagnetized electrons). Several data points where u_e was computed to be small in this study violated the first limitation, which suggests that, in practice, the uncertainty of u_e with this technique will not allow the total collision frequency to be calculated meaningfully at times of negligible electron current. No instances of the second requirement being violated were observed. Consequently, we can conclude that the proposed technique for computing ν_t is sensitive to uncertainty in u_e but tolerant of the uncertainty in \mathcal{E} , and this sensitivity imposes an analytical obstacle in determining ν_t when u_e is small.

Since the method applied here involves numerically integrating the ion density gradient starting at the boundary established by Faraday probe measurements, another assumption is that the technique is not overly sensitive to uncertainty in those boundary measurements. Here, we examine this sensitivity due to random and systematic variations in the boundary conditions. Physically, this is to say that the boundary density values could be noisy or uniformly skewed in time, which could lead to unstable numerical solutions via the integration technique described in Sec. II B. With regard to random fluctuations of the boundary value, even though the Faraday probe signal unavoidably carried random noise of up to 5% (capturing 95% of the normally distributed noise), stable solutions for n , E_z , and n_0 were still found. This suggests that the numerical scheme was relatively insensitive to random noise in the boundary conditions. This is also true for systematic uncertainty, as demonstrated by Fig. 9 which shows the mean spatial change in ion density as the boundary density is uniformly varied. The trend is representative of all phases. The figure indicates that the system is a sensitive, non-linear function of boundary density, yet the smoothness of the curve implies that the numerical solver is still stable over a wide range. If the numerical scheme went unstable for certain systematic increases in the boundary conditions, we would expect the curve in Fig. 9 to be non-monotonic. In total, there is evidence that the numerical scheme is stable in the face of random and systematic variations in the boundary conditions, and thus, the computed quantities are reliable. We also reiterate here that although the breathing frequency was lower during the Faraday probing compared to the TRLIF measurements (see Fig. 3), the

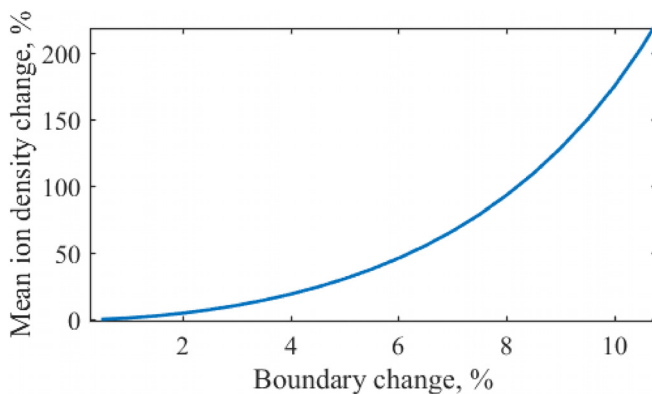


FIG. 9. The mean change in ion density as a function of the uniform increase in the boundary density.

oscillations were qualitatively similar so we do not expect the shape of the boundary density signal to be misrepresented.

Another assumption that must be evaluated is current continuity—namely, that electron current density can be inferred from the total and ion current densities. This assertion relies on two assumptions: that the total current density can be found by dividing the total discharge current by the channel area and that radial distribution of current is not fluctuating significantly in time. Violations of both of these assumptions may help explain some of the spurious results we found in Sec. IV. As mentioned there, several values of ν_t were calculated to be below the local classical collision frequency. Some of these physical discrepancies were explainable within the error of the measurements, while others were not. For example, at $z/L = -0.4^\circ$ and 188° , the total collision frequency is only 34 kHz below the classical value, which is explainable within the ~ 10 MHz average uncertainty in ν_t at the location. But at $z/L = -0.05^\circ$ and 228° , the difference is several orders of magnitude greater than the local uncertainty. In these cases, the issue stems from the calculation of j_e , which must be close to zero or somewhat negative according to current continuity when ν_t becomes very small. A possible explanation is that at these points the average total current density is a poor representation of the relevant (centerline) current density. In particular, the fact that j_e is implausibly small at these points indicates that the radial current density profile most likely narrows here such that the total discharge current is distributed over an area smaller than that dictated by the channel geometry. We can assess the impact of this radially uniform assumption more quantitatively with a sensitivity analysis. Since quasi-neutrality is assumed and n has been measured on the centerline, the current distribution controls u_e on the centerline via the relation $u_e = j_e/n = (j_d - j_i)/n$. Indeed, in the one-dimensional case, we can determine from Eq. (3)

$$\frac{\partial \nu_t}{\partial u_e} = \Omega \frac{\omega_{ce}}{u_e} - \frac{\nu_t}{u_e} \quad (11)$$

the sensitivity of ν_t to changes in u_e . For the region of interest, $\omega_{ce} > \nu_t$ such that the last term in the above equation can be ignored. In this case, changes in ν_t are inversely proportional to ν_t itself and directly proportional to the fractional change in u_e . This suggests that the lower ν_t values are more susceptible to uncertainty due to a non-uniform current distribution than the larger values for a given uncertainty in u_e since $\partial \nu_t / \partial u_e$ will be large. This may help explain why ν_t was lower than ν_{class} in some instances. Further, it suggests that the lower limit of the measured ν_t is strongly dependent on the assumed current distribution, and thus, a more rigorous way of determining the distribution—such as by measuring j_i at multiple radial locations throughout the channel—is necessary to fully resolve the lower extent of the fluctuations in ν_t . To illustrate this, Fig. 10 shows the time-averaged total collision frequency for three assumed current distributions: uniform, linear from each wall to the channel centerline, and Gaussian with a variance of $w^2/4$. These cases represent the limits on realistic current profiles: maximum convexity, zero convexity, and in between, respectively. In this way, these cases provide bounds for the true total collision frequency and illustrate the effect of assuming non-uniform

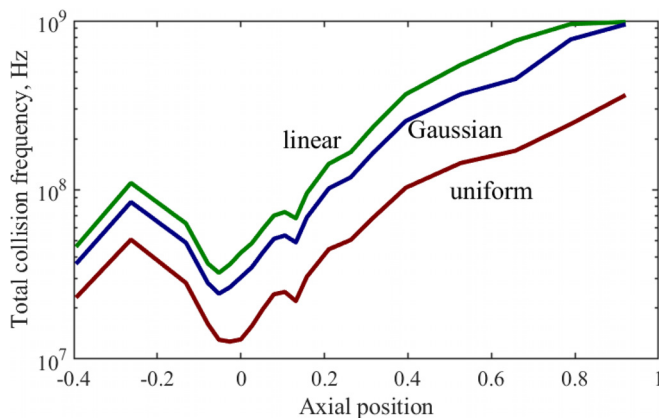


FIG. 10. The time-averaged total collision frequency for different assumed current distributions: uniform, linear, and Gaussian.

current distributions. Naturally, the greater the convexity a profile has the lower the centerline current density can be to achieve a certain discharge current. As a result, more convex profiles have smaller centerline values for j_d and thus smaller j_e and u_e , and so, a smaller electron cross-field collision frequency is computed. Although there is considerable variability in ν_t due to the effect exemplified by Fig. 10, the minimum ν_t occurring at the trough in discharge current is still at most comparable to ν_{class} for any assumed distribution. However, the spatial extent over which $\nu_t \lesssim \nu_{class}$ does vary considerably for different current distributions. At the phase of minimum discharge current (see Fig. 6), ν_t was within an order of magnitude of ν_{class} for 84%, 37%, and 42% of the measurement domain for the uniform, linear, and Gaussian distributions, respectively. With this in mind, one of the conclusions of Sec. IV—that classical collisions may dominate at certain phases—still holds for some locations in the channel within the certainty of the measurements regardless of the current distribution. Alternatively, a vanishing axial electron current may not be a sign that the assumed current distribution is incorrect but may simply be an indication that the electrons are diverging from the centerline within the measurement domain, and thus, the one-dimensional Ohm's law used in this technique is inappropriate. This explanation seems likely given that j_e tended to approach zero at the downstream end of the measurement domain, where electrons may still be diverging from the cathode.

Finally, we consider *a posteriori* the necessity of a generalized Ohm's law, including electron pressure and ion resistivity, in Sec. II B. As Fig. 7 shows, the electron pressure gradient is nearly comparable to the accelerating electric field strength at many phases and locations. As a result, \mathcal{E} cannot be approximated with E_z and thus the inclusion of electron pressure is important. However, ion resistivity tends to be small, although it can become important when the electric field weakens far upstream and downstream. Even though it is never a dominating term, this study indicates that it is at least non-negligible.

C. Relation between breathing and anomalous transport

The observation that anomalous transport varies with breathing oscillations agrees with experimental and numerical studies in the literature. Adam *et al.* observed enhanced transport in an axial-azimuthal PIC simulation which was attributed to the electron cyclotron drift instability (ECDI), a kinetic effect in which energy from the large electron drift velocity in the acceleration region feeds a wave via inverse cyclotron resonance.⁸ These simulations also resolved breathing oscillations and demonstrated that the fluctuating electric field due to the ECDI correlated with them. Likewise, PIC simulations by Coche and Garrigues indicated that the cross-field electron mobility profile fluctuates during a breathing cycle and that the profile increases at peaks in the discharge current that correspond with the onset of azimuthal instabilities (ECDI).³⁹ Recently, Tsikata *et al.* experimentally observed that in some discharge voltage regimes there is strong correlation between the discharge current and the strength of the ECDI electric field fluctuations.⁴⁰ That study also involved kinetic simulations that reflected the same trends. Although our present study cannot identify the mechanism behind the quantified anomalous transport, it similarly shows correlation between anomalous transport and the breathing mode and, in fact, shows the anomalous collision frequency varying by orders of magnitude over a breathing cycle.

One of the major implications of this relationship between electron transport and low-frequency oscillations is that the anomalous collision frequency must be simulated dynamically to accurately capture electron transport. Many modern fluid electron simulations employ spatially fixed transport profiles.^{19,41} According to the findings of the present study, that approach—especially when using empirically derived steady profiles—is not valid. Anomalous transport fluctuates by orders of magnitude on the time scale of breathing oscillations, and thus, a steady profile is inappropriate. Further, this study has revealed that many quantities fluctuate significantly during a breathing cycle along with the anomalous collision frequency. For instance, the maximum peak-to-peak variation is 52% for ion density, 142% for ion velocity, 185% for electron temperature, and 346% for electric field. This may suggest that electron transport is sensitive to some of these quantities, which is consistent with ECDI.⁷

VI. CONCLUSIONS

The goal of this experiment was to demonstrate a technique for measuring electron anomalous collision frequency over time and from these measurements determine the relationship between anomalous electron transport and low-frequency breathing oscillations. To do this, TRLIF measurements were made inside and in the near plume of a Hall thruster, and Faraday probe measurements were made at a single downstream location. Using moments of the Boltzmann equation, these data were sufficient to compute density, ionization rate, and electric field throughout the TRLIF domain. Further, neutral continuity and momentum conservation equations yielded the neutral density as well. With this information, the total electron

collision frequency was calculated as a function of axial position and breathing phase.

The average profiles generated in this experiment were qualitatively realistic and indicated that anomalous collisions dominated over the entire probed domain. However, the time-resolved results showed that the anomalous collision frequency profile varies significantly over a breathing cycle. In fact, at certain phases, classical collisions may dominate as the electron transport mechanism.

A major insight gained from these measurements is that the fluctuation of the anomalous collision frequency over a breathing cycle impacts the time-averaged electron transport and cannot be accurately captured with a steady profile. In the absence of a first-principles anomalous electron transport model, a time-resolved treatment of anomalous collisions must be included in numerical simulations to truly capture the electron dynamics in the presence of low-frequency oscillations. By extension, these oscillations themselves must be simulated accurately to accomplish this.

ACKNOWLEDGMENTS

This work was supported by NASA Space Technology Fellowship NNX14AL65H. E. Dale would like to thank Matthew Byrne for his assistance in carrying out the laser measurements discussed in this paper and Sarah Cusson and Marcel Georgin for proofreading this manuscript.

REFERENCES

- ¹D. Y. Oh, J. S. Snyder, D. M. Goebel, R. R. Hofer, and T. M. Randolph, *J. Spacecr. Rockets* **51**, 1822 (2014).
- ²R. R. Hofer, J. E. Polk, M. J. Sekerak, I. G. Mikellides, H. Kamhawi, T. R. Sarver-Verhey, D. A. Herman, and G. Williams, in *Proceedings of 52nd AIAA/SAE/ASEE Joint Propulsion Conference* (American Institute of Aeronautics and Astronautics, Salt Lake City, UT, 2016).
- ³J.-P. Boeuf, *J. Appl. Phys.* **121**, 011101 (2017).
- ⁴T. Randolph, V. Kim, H. Kaufman, K. Kozubsky, V. Zhurin, and M. Day, in *Proceedings of 23rd International Electric Propulsion Conference* (IEPC-93-93, 1993).
- ⁵A. I. Morozov, Y. V. Esipchuk, and G. N. Tilinin, *Sov. Phys. - Tech. Phys.* **17**(1), 38-45 (1972).
- ⁶M. S. McDonald, C. K. Bellant, B. A. S. Pierre, and A. D. Gallimore, in *Proceedings of 47th AIAA/ASME/SAE/ASEE Joint Propulsion Conference & Exhibit* (American Institute of Aeronautics and Astronautics, San Diego, CA, 2011).
- ⁷T. Lafleur, S. D. Baalrud, and P. Chabert, *Phys. Plasmas* **23**, 053503 (2016).
- ⁸J. C. Adam, A. Héron, and G. Laval, *Phys. Plasmas* **11**, 295 (2004).
- ⁹J. W. Koo and I. D. Boyd, *Phys. Plasmas* **13**, 033501 (2006).
- ¹⁰J. M. Haas, "Low-perturbation interrogation of the internal and near-field plasma structure of a Hall thruster using a high-speed probe positioning system," Ph.D. thesis (University of Michigan, 2001).
- ¹¹D. Staack, Y. Raitses, and N. J. Fisch, *Rev. Sci. Instrum.* **75**, 393 (2004).
- ¹²B. A. Jorns and R. R. Hofer, *Phys. Plasmas (1994-present)* **21**, 053512 (2014).
- ¹³L. Grimaud, A. Petin, J. Vaudolon, and S. Mazouffre, *Rev. Sci. Instrum.* **87**, 043506 (2016).
- ¹⁴I. G. Mikellides, B. Jorns, I. Katz, and A. Lopez Ortega, in *Proceedings of 52nd AIAA/SAE/ASEE Joint Propulsion Conference* (American Institute of Aeronautics and Astronautics, Salt Lake City, UT, 2016).
- ¹⁵I. G. Mikellides and A. Lopez Ortega, *Plasma Sources Sci. Technol.* **29**, 014003 (2010).
- ¹⁶E. Y. Choueiri, *Phys. Plasmas (1994-present)* **8**, 1411 (2001).
- ¹⁷J. Bareilles, G. J. M. Hagelaar, L. Garrigues, C. Boniface, J. P. Boeuf, and N. Gascon, *Phys. Plasmas* **11**, 3035 (2004).
- ¹⁸J. P. Boeuf and L. Garrigues, *J. Appl. Phys.* **84**, 3541 (1998).
- ¹⁹G. J. M. Hagelaar, J. Bareilles, L. Garrigues, and J. P. Boeuf, *J. Appl. Phys.* **91**, 5592 (2002).
- ²⁰F. I. Parra, E. Ahedo, J. M. Fife, and M. Martínez-Sánchez, *J. Appl. Phys.* **100**, 023304 (2006).
- ²¹I. G. Mikellides and I. Katz, *Phys. Rev. E* **86**, 046703 (2012).
- ²²J. A. Linnell and A. D. Gallimore, in *Proceedings of 31st International Electric Propulsion Conference*, Ann Arbor, MI (2009), IEPC-2009-105.
- ²³W. A. Hargus and M. A. Cappelli, *J. Propul. Power* **18**, 159 (2002).
- ²⁴D. Goebel and I. Katz, *Fundamentals of Electric Propulsion: Ion and Hall Thrusters* (John Wiley & Sons, 2008), Vol. 1.
- ²⁵J. Perez-Luna, G. J. M. Hagelaar, L. Garrigues, and J. P. Boeuf, *Plasma Sources Sci. Technol.* **18**, 034008 (2009).
- ²⁶W. Huang, A. D. Gallimore, and R. R. Hofer, *J. Propul. Power* **27**, 553 (2011).
- ²⁷S. Mazouffre, G. Bourgeois, L. Garrigues, and E. Pawelec, *J. Phys. D: Appl. Phys.* **44**, 105203 (2011).
- ²⁸J. W. Dankanich, M. Walker, M. W. Swiatek, and J. T. Yim, *J. Propul. Power* **33**, 668 (2017).
- ²⁹R. Hofer, S. Cusson, R. Lobbia, and A. Gallimore, in *Proceedings of 35th International Electric Propulsion Conference* (2017), IEPC-2017-232.
- ³⁰S. Cusson, R. Hofer, R. Lobbia, B. Jorns, and A. Gallimore, in *Proceedings of 35th International Electric Propulsion Conference* (2017), IEPC-2017-239.
- ³¹M. J. Sekerak, A. D. Gallimore, D. L. Brown, R. R. Hofer, and J. E. Polk, *J. Propul. Power* **32**, 903 (2016).
- ³²W. Huang, B. Drenkow, and A. Gallimore, in *Proceedings of 45th AIAA/ASME/SAE/ASEE Joint Propulsion Conference & Exhibit, Joint Propulsion Conferences* (American Institute of Aeronautics and Astronautics, 2009).
- ³³S. Mazouffre, *Plasma Sources Sci. Technol.* **22**, 013001 (2013).
- ³⁴B. Jorns, C. A. Dodson, J. R. Anderson, D. M. Goebel, R. R. Hofer, M. J. Sekerak, A. L. Ortega, and I. G. Mikellides, in *Proceedings of 52nd AIAA/SAE/ASEE Joint Propulsion Conference and Exhibit* (American Institute of Aeronautics and Astronautics, 2016).
- ³⁵N. A. MacDonald, M. A. Cappelli, and W. A. Hargus, *Rev. Sci. Instrum.* **83**, 113506 (2012).
- ³⁶R. Hofer, D. Goebel, I. Mikellides, and I. Katz, in *Proceedings of 48th AIAA/ASME/SAE/ASEE Joint Propulsion Conference & Exhibit* (American Institute of Aeronautics and Astronautics, Atlanta, GA, 2012).
- ³⁷L. Grimaud and S. Mazouffre, *Plasma Sources Sci. Technol.* **26**, 055020 (2017).
- ³⁸V. H. Chaplin, B. A. Jorns, A. Lopez Ortega, I. G. Mikellides, R. W. Conversano, R. B. Lobbia, and R. R. Hofer, *J. Appl. Phys.* **124**, 183302 (2018).
- ³⁹P. Coche and L. Garrigues, *Phys. Plasmas* **21**, 023503 (2014).
- ⁴⁰S. Tsikata, A. Heron, and C. Honore, in *Proceedings of 35th International Electric Propulsion Conference* (2017), IEPC-2017-443.
- ⁴¹R. Hofer, I. Katz, D. Goebel, K. Jameson, R. Sullivan, L. Johnson, and I. Mikellides, in *Proceedings of 44th AIAA/ASME/SAE/ASEE Joint Propulsion Conference & Exhibit* (American Institute of Aeronautics and Astronautics, Hartford, CT, 2008).